Superconducting Notch Filter for RFI Mitigation in Ground-Based Radio Telescope

Charles J. Turner, Thomas Stevenson, Robin Cantor, *Senior Member, IEEE*, Lawrence Hilliard, Thomas E. Murphy, *Senior Member, IEEE*, and Berhanu Bulcha

***Abstract*—This article presents a high-rejection, thin-film high-temperature superconductor, microstrip bandstop filter to prevent a local, and high-power radio-frequency interference (RFI) source from interfering with NASA Goddard Geophysical Astronomical Observatory (GGAO)'s very long baseline interferometry (VLBI) global observing system (VGOS) cryogenic receiver. This filter has an excellent 2.7%, 50-dB-fractional-bandwidth, and a center stopband frequency of 9.41 GHz. It does not contain any narrow or interdigital features as found in some designs, which reduces the fringing electric fields and improves its power handling capability. The YBCO films were grown on 435-μm-thick R-plane sapphire substrate and the anisotropic behavior was modeled and simulated with a high degree of accuracy. The device was tested while cooled to 77 K and the measurements agree well with simulation.**

***Index Terms*—Bandstop filters, high-temperature superconductors, radio astronomy.**

I. Introduction

RADIO-FREQUENCY interference (RFI) mitigation can have a critical impact on the performance of receivers used for radio astronomy. Cryogenic receivers provide the necessary sensitivity to detect weak RF signals of galactic origin, but are especially susceptible to local RFI [1], [2]. Very long baseline interferometry (VLBI) is a high angular resolution geodetic technique that uses cosmic radio sources as a reference to accurately measure global reference frames and monitor Earth's orientation and variations. VLBI Global Observing System (VGOS) is the next-generation network of 12 m telescopes that provide broadband receiver systems with four frequency bands ranging from 2 to 14 GHz and high data rates to achieve a measurement accuracy of 1 mm in station position and 0.1 mm/year in station velocity on global scales [2], [3]. The Goddard Geophysical Astronomical Observatory (GGAO) is home to one of these VGOS helium-cooled receivers in Greenbelt, MD. Colocated approximately 110 m from this receiver, the satellite laser ranging (SLR) system uses a 9.4 GHz radar to detect and prevent accidental illumination of overhead aircraft [4]. Under certain orientations, the VLBI receiver will measure one of the radar's sidelobes. This scenario will saturate the front-end low-noise amplifier (LNA) and compromise receiver sensitivity, as well as potentially damage sensitive electronics. The presence of this interfering source imposes constraints on the dish orientation, sky coverage, and schedule; limiting both the scope and duration of observations.

Fortunately, the RFI falls between the various observation bands of this radio telescope and a suitable band rejection filter prior to the LNA would both protect sensitive electronics and enable uninterrupted full-sky observation. In our demonstrated filter, high-temperature superconductor (HTS) planar circuits are used to minimize insertion loss in the passband and meet a strict form factor of 25 mm width, 32 mm length, and 6 mm height to fit in available space inside the existing receiver dewar. This notch filter must handle the higher power radar sidelobe without a change in performance and requires at least 50 dB of signal rejection over 250 MHz of bandwidth with the stopband centered on 9.4 GHz. To the best knowledge of the authors, no published HTS planar notch filter design has demonstrated a 50 dB fractional bandwidth of 2.7% in measurement.

We report here a notch filter realized in thin-film YBCO microstrip capable of rejecting a high-power local RFI source. The filter design consists of seven modified hairpin resonators where the arms are folded to increase parallel coupling. The self-coupled hairpin resonator geometry provides the necessary shunt reactance to achieve higher stopband rejection, demonstrates good quality factors to avoid significantly increasing insertion loss in the observation bands, and avoids the use of narrow-width microstrip or interdigital features. Current concentration at the resonator edges are the limiting factor in power handling capacity of HTS filters [5]. Using small features as in some other designs [6], [7] increases the amount of fringing electric fields along the microstrip edges and risks degrading the filter's performance while exposed to the local, high-power RFI source.

HTS filters have been employed in radio astronomy receivers in the past [8]. However, thin-film HTS notch filter designs are relatively neglected compared to their bandpass counterparts. Other resonator geometries have been measured at high external quality-factors, but impose an increased risk for this application due to their small features, such as interdigital fingers or narrow meander lines [9], [10], [11], [12], [13], [14]. HTS bulk disk

Manuscript received 1 November 2022; revised 25 January 2023; accepted 4 February 2023. Date of publication 9 February 2023; date of current version 23 February 2023. This article was recommended by Associate Editor S. Anlage. *(Corresponding author: Charles J. Turner.)*

Charles J. Turner and Thomas E. Murphy are with the Department of Electrical and Computer Engineering, University of Maryland, College Park, MD 20742 USA (e-mail: cjturner@umd.edu).

Thomas Stevenson, Lawrence Hilliard, and Berhanu Bulcha are with the NASA Goddard Space Flight Center, Greenbelt, MD 20771 USA.

Robin Cantor is with the President and Founder of STAR Cryoelectronics, Santa Fe, NM 87508 USA.

Color versions of one or more figures in this article are available at https://doi.org/10.1109/TASC.2023.3243492.

Digital Object Identifier 10.1109/TASC.2023.3243492

and patch resonators have demonstrated higher power-handling capabilities [15], [16], [17], but in practice these bulkier resonators would not allow us to simultaneously achieve the quality factor, 50 dB fractional bandwidth, and volume requirements. Although not essential for this application, this filter layout is compatible with and could be modified by other filter design techniques such as defected ground structure [18] and cul-de-sac coupling configuration [19] to tailor its performance to other requirements.

II. Bandstop Filter Design

A. Materials

We selected 300 nm thin film YBCO on 435 μm thick R-plane sapphire substrate. This process achieved good epitaxial growth of YBCO and results in high-quality films to minimize surface resistivity. The selected substrate thickness and filter layout ensures a wide safety margin between the simulated current density and critical current density of the YBCO, such that the device could reliantly handle a 1 Watt RFI signal with 50 Ω microstrip transmission lines when cooled to 20 K. R-plane sapphire provides low-dielectric losses and high thermal conductivity, but requires accurate electromagnetic (EM) simulation to address its anisotropic permitivity [20]

$$\varepsilon_r = \begin{bmatrix} 10.0842 & -0.7842 & 0.7038 \\ -0.7842 & 10.0842 & -0.7038 \\ 0.7038 & -0.7038 & 9.9316 \end{bmatrix}.$$

The 3-D EM model incorporates this anisotropic permittivity matrix and is simulated through Ansys HFSS. In order to prevent a simulation error caused by the negative values in this permitivity matrix, it is necessary to insert a thin isotropic buffer ($\varepsilon_r = 10$) on the ends of the anisotropic substrate and de-embed the waveports. The filter layout's orientation on the substrate could result in a frequency-shift of the stopband and the EM model enabled us to accurately predict the impact of fabrication tolerances. At an ideal orientation, the simulation results agreed with an equivalent isotropic model with no noticeable impact to the field line behavior or scattering parameters. However, rotating the filter layout near its optimal orientation results in approximately a 15 MHz shift per degree of rotation. Multiple design variations were produced on the wafer layout where the outer arm of the resonator was adjusted by increments of 25 μm to ensure a usable filter for the receiver in the first fabrication run.

B. Circuit

Fig. 2 illustrates the design layout and defines its physical dimensions. This filter design requires a 50-dB fractional bandwidth greater than 2.7%, and a 3-dB fractional bandwidth less than 5.3% to maximize stopband RFI signal rejection and minimize passband insertion loss. Chebyshev values for a seven-element notch filter circuit set each element's required reactance slope values and external Q-factor (Q_e) values as large as 845 Ω and 35, respectively [21]. These relatively large values can be difficult to physically realize with planar microstrip. A

Fig. 1. Photo of the 12 m GGAO VGOS antenna (courtesy of NASA SGP).

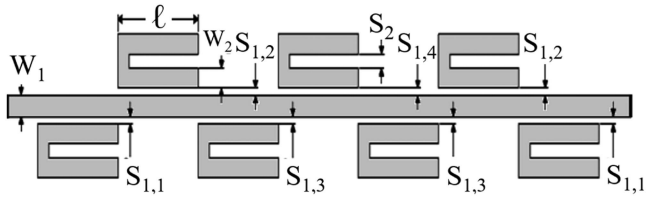

Fig. 2. Layout of microstrip self-coupled hairpin resonator notch filter design.

typical planar microstrip notch filter design consists of a series of coupled half-wavelength resonators, each positioned a quarter-wavelength apart (with respect to the filter's center frequency ω_0) along the direction of propagation [21]. However, these designs limit coupling between the length (l) of the resonator and transmission line, making it difficult to achieve a larger coupling capacitance. Decreasing the gap (S_1) between the resonator and the transmission line will increase this capacitance, but only at the expense of decreasing (Q_e)

$$\omega_0^2 = \frac{1}{LC} = \frac{1}{L(C_1 + C_2)} = \frac{\beta^2}{LC_1} \tag{1}$$

$$X(\omega) = \frac{1 - \omega^2 L(C_1 + C_2)}{j\omega C_1(1 - \omega^2 LC_2)} \tag{2}$$

$$x = \frac{\mathrm{d}X(\omega)}{\mathrm{d}\omega}\frac{\omega_0}{2} = \alpha\omega_0 L. \tag{3}$$

When $\Delta\omega = |\omega_0 - \omega| \ll \omega_0$

$$|S_{21}| \approx \left[1 + \left(\frac{1}{4(x/Z_0)}\frac{\omega_0}{\Delta\omega}\right)^2\right]^{-1/2} \tag{4}$$

$$Q_e = \alpha\frac{2}{R}\sqrt{\frac{L}{C}} \tag{5}$$

Where

$$\alpha = \left(1 - \frac{C_2}{C}\right)^{-2}, \beta = \sqrt{1 - \frac{C_2}{C}}. \tag{6}$$

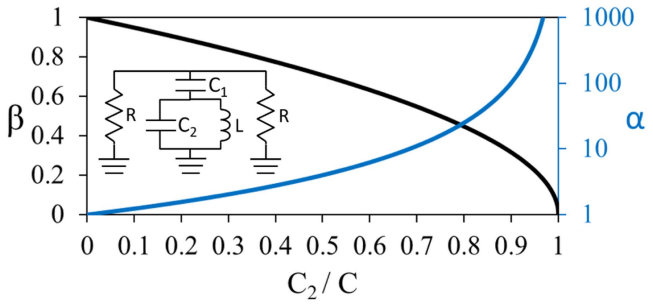

Fig. 3. Equivalent lumped circuit model for self-coupled hairpin resonator. When the sum $C_1 + C_2$ is held constant, the slope reactance and external quality factor will scale proportional to α.

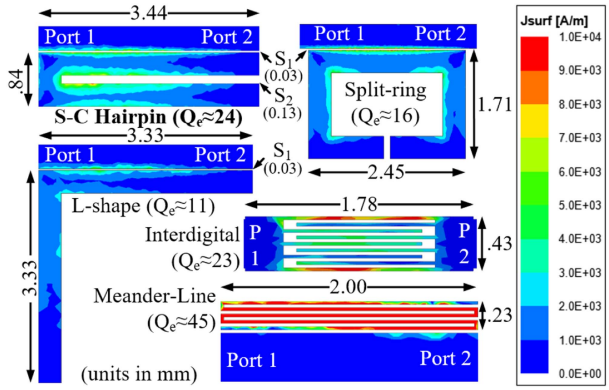

Fig. 4. Current density for various microstrip resonator geometries.

The lumped element circuit in Fig. 3 approximates the response of the edge-coupled (transmission line to resonator), self-coupled (between resonator arms), hairpin resonator close to its resonant frequency. Folding the microstrip resonator introduces a parallel capacitance between its arms. The effect is equivalent to introducing a capacitance C_2 in parallel to the shunt inductance L in a lumped RLC circuit. If R, L, and $C = C_1 + C_2$ are held constant, the resonant frequency ω_0 holds as C_2 increases and C_1 decreases. It also increases the reactance slope, insertion loss near the resonant frequency, and external quality factor as described by (1)–(6). Equation (1) equivalently describes both the resonant frequency for a common shunt RLC circuit and the depicted circuit with the given circuit parameter definitions. Equations (2) and (3) define the circuit reactance and reactance slope, respectively. Finally, (4) and (5) account for the insertion loss (or signal rejection) at frequencies near the resonant frequency and the external quality factor of the resonator.

Fig. 3 also illustrates the change in α and β as C_2/C is increased. The reactance slope and quality factor are proportional to α and increasing the reactance slope will increase the signal rejection at frequencies close to ω_0. An additional advantage to this shunt circuit element is that as C_2/C increases, β decreases, and reduces the effect a change in coupling capacitance to the resonator (ΔC_1) would have on a change in the resonator's center frequency ($\Delta\omega_0$). This artifact reduced the number of EM simulation model parameters and simplified the optimization process for the final filter design. Using this shunt circuit element enables us to choose inductance and capacitance values which meet the necessary reactance slopes of the Chebyshev filter model and can be realized with 50 Ω microstrip resonators.

C. Layout and EM Simulation

Fig. 4 shows the current density maps for a selection of various resonator geometries, which were investigated for an applied 1 Watt of power at 9.4 GHz. The smaller feature sizes of the interdigital or meander-line resonators result in more fringing electric fields and increased current density, increasing the current density beyond the targeted safety margin from the estimated critical current density. The L-shape and split-ring resonator examples had a lower Q_e (set to an equivalent coupling gap) and realized with 50 Ω transmission line. The split-ring resonator Q_e can be increased, but at the expense of expanding its width perpendicular to the transmission line. We chose the self-coupled hairpin resonator and set the gap at 127 μm as a tradeoff between higher Q_e and lower current density.

Fig. 5 shows the ADS simulation results for a microstrip circuit model of the self-coupled hairpin resonator at different gaps between arms and compares it with microstrip circuit models of the L-shape and split-ring resonators. Observing the Q_e plot, S_2 is chosen for the range of achievable Q_e values while considering the current density from EM simulation. To physically realize the filter circuit, the appropriate values of S_1 are chosen from this plot. The $\Delta\omega_0$ plot highlights the additional advantage of decreasing the coupling gap between resonator arms. When S_2 is decreased, the change in resonant frequency also decreases with changing S_1. This resulted in a closer agreement between circuit and EM simulation and reduced the simulation time and number of physical parameters that needed to be optimized.

Ansys HFSS provided 3-D EM modeling and simulation of this filter design to account for the anisotropic substrate and minor parasitic impedances not captured in the simplified ADS circuit model. Optimizing the 3-D EM model resulted in the following values as identified in Fig. 2: $w_1 = 381$ μm, $w_2 = 356$ μm, $l = 2.2$ mm, $S_{1,1} = 76$ μm, $S_{1,2} = 38$ μm, $S_{1,3} = S_{1,4} = 25$ μm, and $S_2 = 127$ μm.

III. Fabrication and Measurements

STAR Cryoelectronics performed the fabrication of the filter chips on a 435 μm thick R-plane sapphire wafer. The filter dimensions were patterned on thin-film YBCO with photolithography and the microstrip maintained a minimum 356 × 0.3 μm cross-section. The selected R-plane crystal orientation allowed good quality epitaxial growth of YBCO films and the substrate thickness was important for achieving 50 Ω transmission lines with physically realizable feature dimensions. For this application, the cryogenic receiver is cooled by compressed helium to 20 K and the T_c of YBCO is approximately 93 K, providing a buffer region of around 73 K. The film quality, cross-section, wafer thickness, operating temperature, and resonator geometry enhances its capability in rejecting higher power RFI at 9.4 GHz without a degradation in performance while measuring the desired radio astronomy signals.

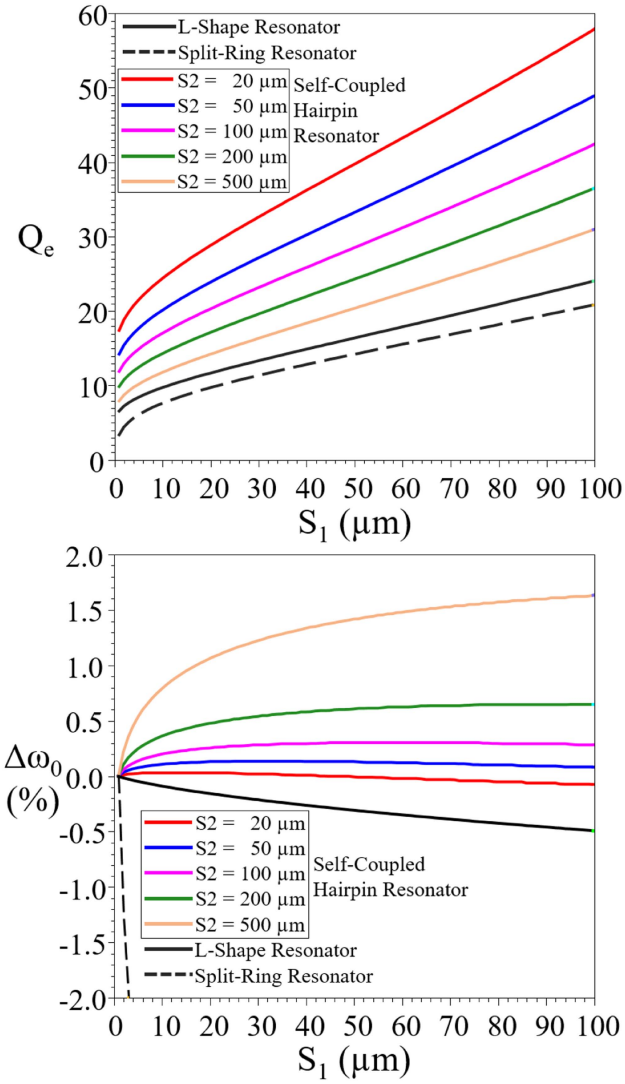

Fig. 5. ADS microstrip circuit model simulations of external quality factor (Q_e) and shift in resonant frequency ($\Delta\omega_0$) for various resonators geometries.

The final EM model incorporated multiple fabrication uncertainties, which could impact filter performance. This included factors such as the circuit layout's orientation and position on the wafer. The sum effect of these various factors could shift the stopband by an amount slightly less than half of the 50 dB fractional bandwidth. In order to ensure successful fabrication of an implementable filter in the first fabrication run, we created multiple design variations where the outer arm of each resonator was lengthened or shortened by 25 μm. Small changes in temperature should not impact the filter's performance. The kinetic inductance in the YBCO film was approximated as less than 0.22 pH/square if operating at or below 20 K. This is a negligible contribution compared to an estimated 180 pH/square for the geometric inductance of the microstrip. As a result, initial testing of the filter was performed with liquid nitrogen (77 K) in a laboratory environment.

After dicing the wafer into chips, the nominal design was selected and epoxied into aluminum housing with a silver epoxy

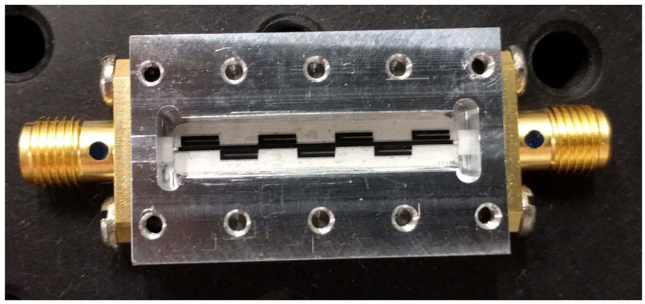

Fig. 6. Packaged notch filter with lid removed.

TABLE I
COMPARISON WITH COMPARABLE BANDSTOP FILTERS

Ref	f_c(GHz)	Δf_{20dB}(%)	Δf_{50dB}(%)
[22]	1.8	0.9	–
[19]	2.0	1.9	–
[23]	14.8	2.9	–
[8]	1.6	7.9	–
[24]	1.4	0.7	0.5
[11]	2.3	1.3	0.8
[10]	2.2	1.8	1.1
[13]	2.0	4.2	1.5
[12]	0.9	7.8	1.5
This Work	**9.4**	**4.3**	**2.7**

(EPO-TEK EJ2189-LV) suitable for cryogenic temperatures. SMA connectors were mounted to each side and the pins were similarly epoxied to 2 μm thick Au bond pads located on each end of the microstrip. Fig. 5 shows a picture of the final device without its lid. We used a Keysight VNA to measure the filter's insertion loss after reaching thermal equilibrium while submerged in liquid nitrogen. The VNA was calibrated for cable loss and stainless steel SMA cables were used to minimize thermal contraction in the cable length.

Fig. 6 provides a plot of the ADS simulation results and measurement. The measured filter achieved the target fractional bandwidth and is compared in Table I to other published notch filter designs. Another noteworthy achievement is that this filter design achieved a higher 50 dB fractional bandwidth, but in some cases a more narrow 20 dB fractional bandwidth than previously reported measurements. This is favorable for our application where we need strong stopband rejection but do not want a deliberately wideband design that overlaps with the observation bands of the radio telescope. The device was tested at approximately 57 K warmer than its intended operating temperature. Modeling the expected insertion loss based on use of the Mattis-Bardeen equation to estimate the quasiparticle dissipation at the actual operating temperature results in an approximate 2 dB insertion loss in the upper passband [25]. The maximum insertion loss in the lower and upper passbands are 0.614 dB and 2 dB, respectively. This loss is attributed to the test environment and impedance mismatch in the connector-to-chip interface as is apparent in the measured return loss as higher frequencies. We anticipate the insertion loss will be reduced in future testing at lower temperatures and in a revised packaging design. The measurement agrees well with simulation and confirms our estimation of kinetic inductance and insertion

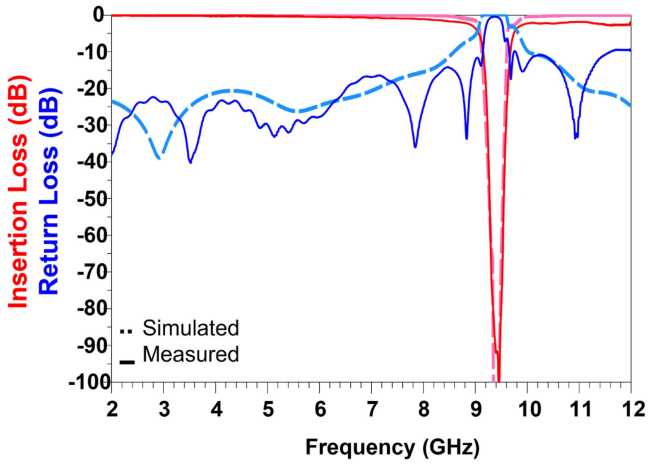

Fig. 7. Comparison of simulated and measured insertion loss and return loss for packaged filter cooled to 77 K.

losses as a function of ambient temperature. In a future effort, we will assemble the filter chips in a new housing design and test these devices under the correct temperature of 20 K. The SMA connectors will also be replaced with 2.92 mm Ka-band connectors to provide improved higher frequency performance and resilience to thermal cycling.

IV. Conclusion

Our team has successfully demonstrated an HTS microstrip notch filter with a significant 50-dB-fractional-bandwidth notch and low insertion loss in a wide passband to meet the described application's strict requirements. The selection of YBCO films, substrate parameters, and resonator geometry were tailored for a consistent filter response while exposed to a local and high-power RFI source. The self-coupled hairpin resonator design enabled us to physically realize the desired filter circuit model using planar microstrip and maintain a compact footprint. We anticipate improvements to the housing design will reduce losses at higher frequencies, making this device an immediately feasible solution for GGAO's VGOS RFI mitigation needs.

Acknowledgment

The authors would like to thank Kongpop U-Yen for providing background knowledge and technical support during his time at NASA Goddard Space Flight Center. The authors would also like to thank Ganesh Rajagopalan at MIT Haystack Observatory for reviewing the filter design, as well as providing technical requirements and guidance to ensure successful integration into the receiver.

References

[1] P. V. Bout, "Interference and radioastronomy," *Phys. Today*, vol. 44, no. 11, pp. 41–49, 1991.

[2] A. Nothnagel, T. Artz, D. Behrend, and Z. Malkin, "International VLBI service for geodesy and astrometry: Delivering high-quality products and embarking on observations of the next generation," *J. Geodesy*, vol. 91, no. 7, pp. 711–721, Jul. 2017.

[3] A. Niell et al., "Demonstration of a broadband very long baseline interferometer system: A. new instrument for high-precision space geodesy," *Radio Sci.*, vol. 53, no. 10, pp. 1269–1291, 2018.

[4] J. F. McGarry et al., "NASA's satellite laser ranging systems for the twenty-first century," *J. Geodesy*, vol. 93, no. 11, pp. 2249–2262, 2019. [Online]. Available: https://link.springer.com/10.1007/s00190-018-1191-6

[5] T. Zhang, J. Du, and Y. J. Guo, "High-TC superconducting microwave and millimeter devices and circuits—An overview," *IEEE J. Microw.*, vol. 2, no. 3, pp. 374–388, Jul. 2022.

[6] L. Gao et al., "8-GHz narrowband high-temperature superconducting filter with high selectivity and flat group delay," *IEEE Trans. Microw. Theory Techn.*, vol. 57, no. 1, pp. 1767–1773, Jul. 2009.

[7] T. Yu et al., "A wideband superconducting filter using strong coupling resonators for radio astronomy observatory," *IEEE Trans. Microw. Theory Techn.*, vol. 57, no. 1, pp. 1783–1789, Jul. 2009.

[8] S. Wallage, J. L. Tauritz, G. H. Tan, P. Hadley, and J. E. Mooij, "High Tc superconducting CPW bandstop filters for radio astronomy front ends," *IEEE Trans. Appl. Supercond.*, vol. 7, no. 2, pp. 3489–3491, Aug. 1996.

[9] H. Liu et al., "Design of high-temperature superconducting wideband bandpass filter with narrow-band notch resonators for radio telescope application," *IEEE Trans. Appl. Supercond.*, vol. 27, no. 4, Jun. 2017, Art. no. 1501704.

[10] Y. Heng et al., "Compact superconducting dual-band bandpass filter by combining bandpass and bandstop filters," *Electron. Lett.*, vol. 49, no. 19, pp. 1230–1232, 2013.

[11] S. Pal, M. J. Lancaster, and R. D. Norrod, "HTS bandstop filter for radio astronomy," *IEEE Microw. Wireless Compon. Lett.*, vol. 22, no. 5, pp. 236–238, May 2012.

[12] P. D. Laforge, R. R. Mansour, and M. Yu, "The use of low-pass filters as impedance inverters for highly miniaturized superconducting bandstop filter designs," *IEEE Trans. Appl. Supercond.*, vol. 21, no. 3, pp. 575–578, Jun. 2011.

[13] A. Corona-Chavez, M. Nogues-Hoyos, L. Esteras-Otal, D. V. Murthy, and B. Sanchez-Rinza, "A high-temperature superconducting notch filter to suppress cellular-band interference in radiotelescopes," *IEEE Trans. Appl. Supercond.*, vol. 21, no. 2, pp. 68–70, Apr. 2011.

[14] Z. Aboush and A. Porch, "Compact, narrow bandwidth, lumped element bandstop resonators," *IEEE Microw. Wireless Compon. Lett.*, vol. 15, no. 8, pp. 524–526, Aug. 2005.

[15] B. Aminov et al., "YBaCuO disk resonator filters operating at high power," *IEEE Trans. Appl. Supercond.*, vol. 9, no. 2, pp. 4185–4188, Jun. 1999. [Online]. Available: https://ieeexplore.ieee.org/document/783947/

[16] X. He et al., "An ultra-narrow band eight-pole dual-mode HTS patch filter," *Physica C: Supercond. Its Appl.*, vol. 469, no. 21, pp. 1925–1929, 2009. [Online]. Available: https://dx.doi.org/10.1016/j.physc.2009.06.010

[17] T. Saito, S. Kodama, T. Saito, S. Ohshima, and A. Saito, "Design of high power handling filter using cascaded quadruplet superconducting bulk resonators," *IEEE Trans. Appl. Supercond.*, vol. 28, no. 4, Jun. 2018, Art. no. 1500704.

[18] T. Zheng et al., "Design of a high-power superconducting filter with novel DGS structures," *IEEE Trans. Appl. Supercond.*, vol. 24, no. 6, Dec. 2014, Art. no. 1500905.

[19] M. Ohira, M. Kanomata, Z. Ma, and X. Wang, "A new microstrip bandstop filter for fully canonical cul-de-sac coupling configuration," in *Proc. IEEE MTT-S Int. Microw. Symp. Dig.*, 2018, pp. 708–711.

[20] F. Aiga, H. Fuke, Y. Terashima, M. Yamazaki, H. Kayano, and T. Hashimoto, "HTS hairpin microstrip filter on r-cut sapphire substrate," *IEEE Trans. Appl. Supercond.*, vol. 13, no. 2, pp. 287–290, Jun. 2003.

[21] J.-S. Hong and M. J. Lancaster, *Microstrip Filters for RF/Microwave*, vol. 7. Hoboken, NJ, USA: Wiley, 2001.

[22] J.-S. Hong et al., "Thin film HTS passive microwave components for advanced communication systems," *IEEE Trans. Appl. Supercond.*, vol. 9, no. 2, pp. 3893–3896, Jun. 1999. [Online]. Available: https://ieeexplore.ieee.org/document/783878/

[23] M. Esmaeili and J. Bornemann, "Microstrip bandstop filters using l- and t-shaped resonators," in *Proc. Asia-Pac. Microwave Conf.*, 2015, pp. 1–3. [Online]. Available: https://ieeexplore.ieee.org/document/7411622/

[24] G. Zhang, M. J. Lancaster, F. Huang, and N. Roddis, "A superconducting microstrip bandstop filter for an L-band radio telescope receiver," in *Proc. 35th Eur. Microw. Conf.*, 2005, vol. 1, pp. 697–700.

[25] D. C. Mattis and J. Bardeen, "Theory of the anomalous skin effect in normal and superconducting metals," *Phys. Rev.*, vol. 111, pp. 412–417, 1958. [Online]. Available: https://link.aps.org/doi/10.1103/PhysRev.111.412